Tungsten Blue Oxide as a Reusable Electrocatalyst for Acidic Water Oxidation by Plasma-Induced Vacancy Engineering

Hanfeng Liang[1*†], Zhen Cao[2†], Chuan Xia[3], Fangwang Ming[1], Wenli Zhang[1], Abdul-Hamid Emwas[4], Luigi Cavallo[2] & Husam N. Alshareef[1*]

[1]Materials Science and Engineering, Physical Science and Engineering Division, King Abdullah University of Science and Technology (KAUST), Thuwal 23955, [2]KAUST Catalysis Center (KCC), King Abdullah University of Science and Technology (KAUST), Thuwal 23955, [3]Department of Chemical and Biomolecular Engineering, Rice University, Houston, TX 77005, [4]Core Labs, King Abdullah University of Science and Technology (KAUST), Thuwal 23955

*Corresponding authors: hanfeng.liang@kaust.edu.sa; husam.alshareef@kaust.edu.sa; [†]H. Liang and Z. Cao contributed equally to this work.

In contrast to alkaline water electrolysis, acidic water electrolysis remains an elusive goal due to the lack of earth-abundant, efficient, and acid-stable water oxidation electrocatalysts. Here, we show that materials with intrinsically poor electrocatalytic activity can be turned into active electrocatalysts that drive the acidic oxygen evolution reaction (OER) effectively. This development is achieved through ultrafast *plasma sputtering,* which introduces abundant oxygen vacancies that reconstruct the surface electronic structures, and thus, regulated the surface interactions of electrocatalysts and the OER intermediates. Using tungsten oxide (WO_3) as an example, we present a broad spectrum of theoretical and experimental characterizations that show an improved energetics of OER originating from surface oxygen vacancies and resulting in a significantly boosted OER performance, compared with pristine WO_3. Our result suggests the efficacy of using defect chemistry to modify electronic properties and hence to improve the OER performance of known materials with poor activity, providing a new direction for the discovery of acid-stable OER catalysts.
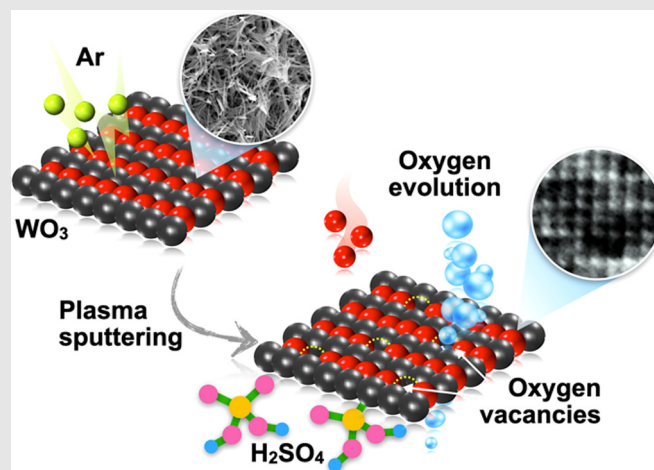
Keywords: WO_3, vacancy engineering, plasma, acidic OER, reusable electrocatalyst

Water electrolysis is a process that can electrocatalytically dissociate water into molecular O_2 via oxygen evolution reaction (OER) and H_2 via hydrogen evolution reaction (HER), which promises an efficient way to produce hydrogen fuel.[1,2] Compared with alkaline conditions, the water electrolysis in acid is preferable because of the higher conductivity (>1.5 times) of protons than hydroxide ions and fewer side reactions.[1,2]

More importantly, the acidic water electrolyzers are readily compatible with commercially available proton-exchange membranes (PEM),[3,4] and thus, possess many advantages, including fast system response, high voltage efficiency, high current density, and high gas purity.[2] While inexpensive, robust, and efficient electrocatalysts are available for both the OER and HER in alkaline electrolytes,[5–11] the only well-established catalysts that can stably drive the OER in acidic media are Ir- and Ru-based noble metal oxides.[12] Ir and Ru are scarce, whereas conventional OER active earth-abundant materials, unfortunately, cannot survive in acidic media due to the anodic corrosion. Developing low-cost and acid-stable OER catalysts, therefore, is highly desirable for not only the widespread implementation of water electrolysis technology but also other half-reactions, including CO_2 and N_2 reduction that are involved in fuel productions.[13,14]

According to the Pourbaix diagram,[15] tungsten oxide (WO_3) is stable in acidic conditions at OER potentials. WO_3 is an n-type semiconductor with good carrier transport and has been widely used in photocatalysis and solar water splitting.[16,17] It has recently demonstrated its efficacy for HER electrocatalysis.[18–20] However, the use of WO_3 for OER electrocatalysis in acidic conditions has not yet been explored. This is perhaps not surprising, as previous computational studies have already revealed that WO_3 is likely inactive for OER due to its very weak binding to OH.[21] Given that the activity is mostly determined by the OER energetics, which is influenced by the interactions of reaction intermediates (i.e., OOH, OH, and O) and catalyst surface active sites,[22,23] it is possible to tune the activity through delicate modification of the interactions. The engineering of vacancies, therefore, offers a promising avenue to improve the activity of catalysts because it could modify the electronic structure and the local coordination chemistry, and consequently, the surface interactions.[24–26] Furthermore, oxygen vacancies in oxides generally lead to an enhanced electrical conductivity[27–30] that promotes the charge transport. Therefore, it is expected that intrinsically catalytically inactive materials such as WO_3 might become OER active through proper vacancy engineering.

Hence, we started with density functional theory (DFT) studies aimed at identifying the impacts of oxygen vacancies on the electronic property and further OER energetics. The WO_3 (001) facet was used for simulations, considering it is the most stable surface. To present a reasonable evaluation, we investigated the surface topology based on the Pourbaix diagram calculation (Supporting Information Figures S1a and S1b) of different types of terminal groups, and we identified the most stable configuration of the WO_3 slab (Supporting Information Figure S1c). We noticed that part of the surface W atoms was not covered by oxygen and could be used as the active OER sites. Thereafter, using this

configuration, we evaluated the critical steps of the OER process by calculating the thermodynamic energetics, following the mechanism proposed previously.[22] The free energy of different adsorbents and the hydrogen were obtained within the computational hydrogen electrode (CHE) framework,[31] where the $H^+ + e^-$ and hydrogen gas were well equilibrated. As demonstrated in Figure 1a (and Supporting Information Figure S2), the step involving the adsorption of OH* on the catalyst surface gives the largest free-energy difference (ΔG_1, 1.98 eV), which is the rate-limiting step determining the overpotential ($\eta = \max\{\Delta G_1, \Delta G_2, \Delta G_3, \Delta G_4\}/e - 1.23$ V). This is in agreement with previous calculations, which show that the OER activity of WO_3 was limited by the weak binding of OH on the surface.[21] Hence, we devised a method to improve the catalytic OER activity by stabilizing the OH* through increasing its binding affinity. Considering that the WO_3 surface is covered by a certain number of oxygen atoms, and the bindings of these negative O^{2-} groups are quite strong, removing some of the surface oxygens should change the electronic structure of the surface W and thereby enhance its binding with other negative groups, such as OH*. We used a simplified prototypical model by removing one surface oxygen atom from the WO_3 model. As expected, such modification affected the electronic structure of the surface W, observable via an electron density difference (EDD) calculation (Figure 1b). Through another systematic calculation of the OER process, we found a much stronger binding of OH*, leading to a lowering of the overpotential by ~250 mV (ΔG_1 decreases from 1.98 to 1.75 eV, Figure 1c). We attributed this improvement to the removal of the highly electronegative terminal group from the stable surface that enhances the binding affinity with other negative groups such as OH*.

The DFT calculations indicated that the vacancy engineering of the catalysts could improve the energetics for OER, suggesting a promising pathway to discover acid-stable OER catalysts. To test this hypothesis, we synthesized WO_3 nanowires with rich oxygen vacancies (WO_3-V_O) and further investigated their OER performance in acidic media. A commonly used method of generating oxygen vacancies involves annealing of precursors at high temperature under reducing atmospheres, which is often accompanied by morphological deformation and particle aggregation,[32] and therefore, could decrease the active surface area. Instead, plasma could induce rapid and efficient surface modification at relatively mild conditions due to its highly active ionic species.[33–36] In this study, we employed Ar plasma to create oxygen vacancies at lower temperatures (Figure 1d). For comparison, WO_3 nanowires with limited oxygen vacancies were also synthesized by annealing the precursor at 300 °C in the air (see Supporting Information "Experimental Section"). It is commonly recognized that creation of vacancies could provide
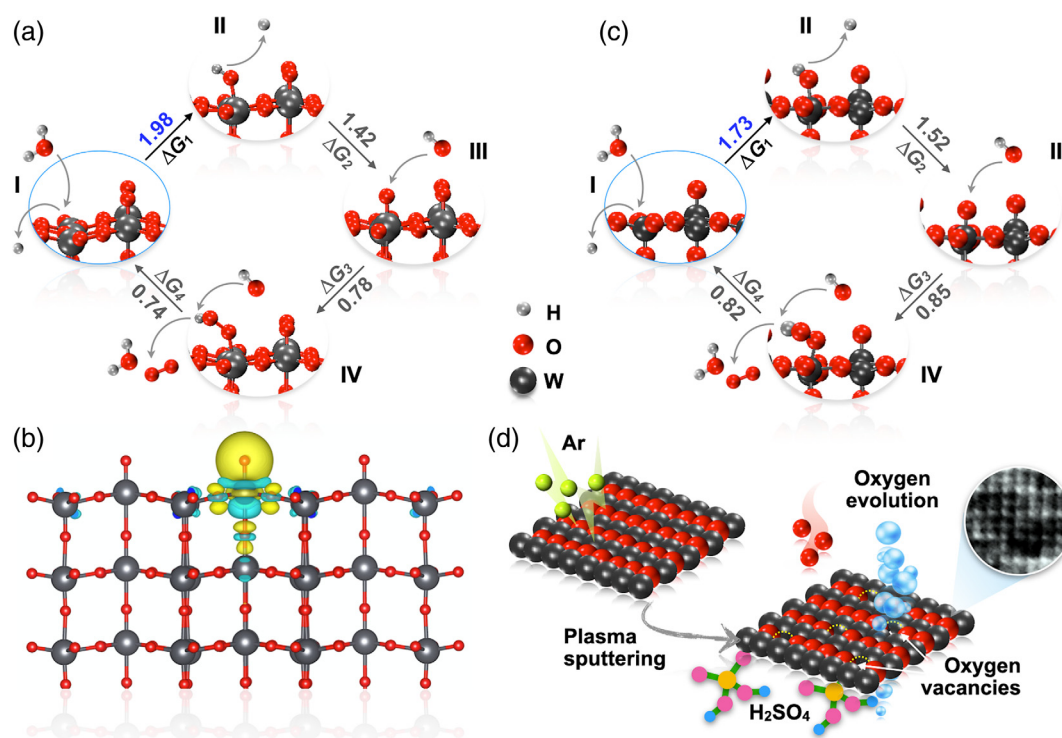
Figure 1. | *OER energetics tuning via oxygen vacancy engineering. (a) OER cycles for the W terminal site of WO₃. (b) Electron density of WO₃-V_O. (c) OER cycles for the W terminal site of WO₃-V_O. (d) Generation of oxygen vacancies in WO₃ by plasma sputtering. The Roman numbers in (a) and (c) indicate the sequence of the OER steps, whereas the ΔG_x presents the Gibbs free energy change during the OER.*

coordinatively unsaturated sites to allow molecular adsorption.[37] Indeed, we observed an intense peak at 531.7 eV in the O 1s X-ray photoelectron spectroscopy (XPS) spectrum of WO_3-V_o (Supporting Information Figure S3) arising from the oxygen species adsorbed at the vacancy sites, a typical feature of oxygen-deficient oxides.[38] Accordingly, part of the W^{6+} in WO_3-V_o was reduced to W^{4+}/W^{5+}. As determined by XPS, the ratio of surface $W^{4+}/W^{5+}/W^{6+}$ is ~0.03/0.37/0.6, corresponding to a chemical formula of $WO_{2.79}$. Notably, the WO_3-V_o was deep blue, whereas the WO_3 was light green, suggesting that the vacancy generation affected the electronic property of the material and therefore its light adsorption (Supporting Information Figure S4). Despite the difference in vacancy concentration, both the WO_3 and WO_3-V_o possessed a hexagonal WO_3 phase according to the X-ray diffraction (XRD) analysis (power diffraction file card #85-2460), and a nanowire morphology. The nanowires are grown along the [001] direction (*c* axis), as determined by the transmission electron microscopy (TEM) characterization (Figure 2a). The anisotropic structure was beneficial in exposing oxygen vacancies on the surface rather than embedding them in bulk. Careful observation revealed that a slight lattice disorder was apparent at the edges (as indicated by the arrows). The atomic image of WO_3-V_o allowed the direct

visualization of the O vacancies (Figure 2b). Numerous small pits were observed (as indicated by the arrows) which could offer more coordinately unsaturated sites for the OER electrocatalysis. The variation in atomic column intensity suggests a variation in the oxygen atomic occupation, indicating the presence of oxygen vacancies. The differences in intensity and contrast are further highlighted in the colored image and the line profile (Figure 2c). Besides, electron paramagnetic resonance (EPR) analysis showed that the WO_3-V_o exhibited a much more intense EPR signal at ~$g = 2.002$, compared with WO_3 (Supporting Information Figure S5), further confirming the presence of a higher concentration of vacancies in WO_3-V_o.[43] The high-angle annular dark-field scanning TEM (HAADF-STEM) analysis revealed that both the W and O were evenly distributed over the nanowire, while the latter was more scattered (Figure 2d). These results, together with the XPS and EPR analyses, confirmed the generation of oxygen vacancies in WO_3-V_o by *plasma sputtering*. In contrast, the crystal lattice of WO_3 was highly ordered even at the edges, and the atomic column intensity was evenly distributed (Supporting Information Figure S6), demonstrating that the vacancy concentration was very low (the O/W ratio is 2.98 based on the XPS analysis, close to the stoichiometric ratio of WO_3, see Supporting Information Figure S3).
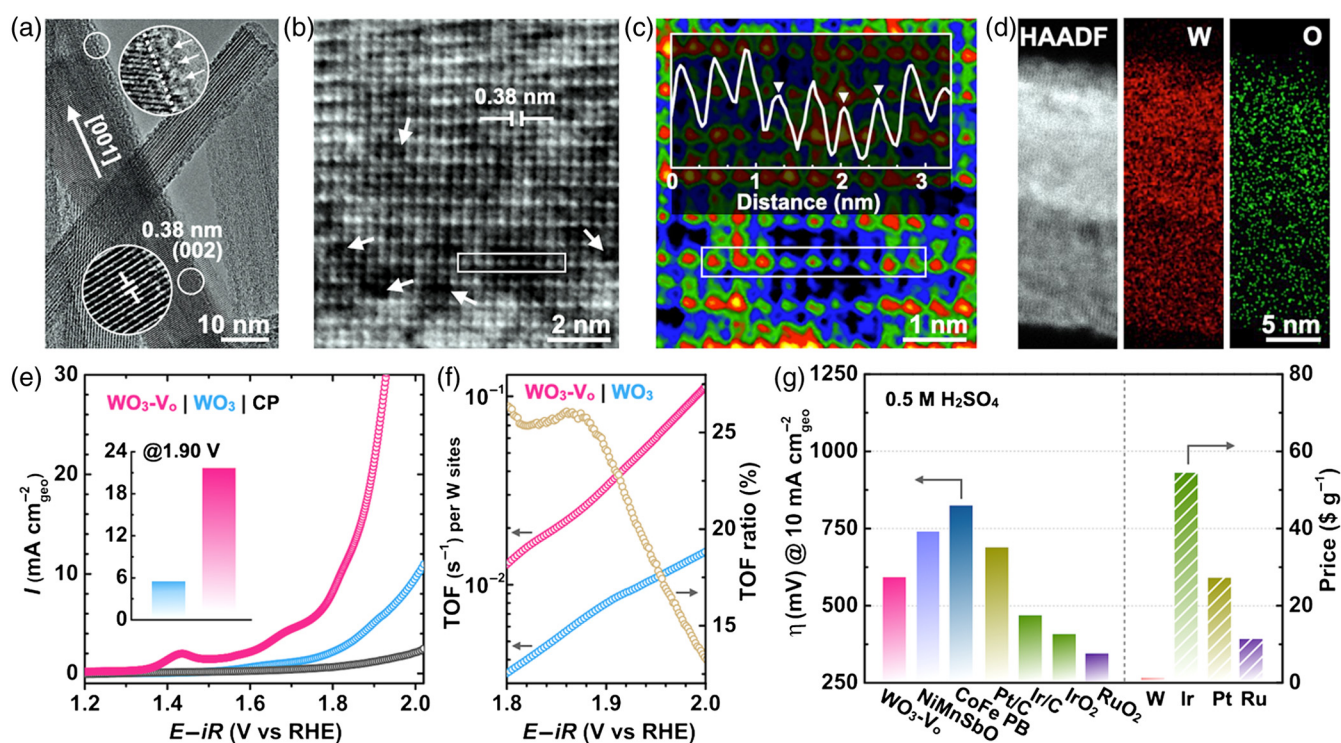
Figure 2. | *Oxygen vacancies boost the electrocatalytic OER activity of WO₃-Vₒ in 0.5 M H₂SO₄. (a and b) TEM images of WO₃-Vₒ. (c) Colored atomic-resolution TEM image with a line profile of nine atoms (indicated by a box). (d) HAADF image and the corresponding elemental maps. (e) LSV curves of WO₃-Vₒ along with WO₃ and CP for comparison. Inset compares the current densities of WO₃-Vₒ and WO₃ at 1.90 V vs RHE. (f) O₂ TOFs over WO₃ and WO₃-Vₒ (left axis) and their relative ratio (right axis). (g) Comparison of the OER performance of various electrocatalysts (Ni₀.₇Mn₀.₃Sb₁.₇Oᵧ in 1.0 M H₂SO₄,[39] CoFe Prussian blue (PB),[40] Pt/C,[41] Ir/C,[42] IrO₂,[42] and RuO₂[41]) in 0.5 M H₂SO₄ and the price of different metals.*

Then we evaluated the OER performance of the WO₃-Vₒ in 0.5 M H₂SO₄ electrolytes. The optimal OER activity was achieved on the WO₃-Vₒ being treated by a 30 s *plasma sputtering* (Supporting Information Figures S7 and S8). A shorter or longer duration would lead to inferior performances of WO₃-Vₒ, though they were, in general, quite close (Supporting Information Figure S8). Figure 2e compares the *iR*-corrected linear sweep voltammetry (LSV) curves of WO₃-Vₒ and WO₃ recorded at 0.5 mV·s⁻¹. We observed several anodic peaks for the WO₃-Vₒ, arising from the oxidation of W⁴⁺/W⁵⁺ species and possibly the oxygen intercalation into the vacancies,[44] whereas the WO₃ had negligible anodic peaks. This suggested that the vacancy engineering tuned the electronic properties, and hence, the oxidation behavior to intensify the electrocatalytic OER performance. Accordingly, the WO₃-Vₒ exhibited a greatly enhanced activity with a current density of 21.3 mA cm⁻² at 1.90 V versus the reversible hydrogen electrode (RHE) (i.e., an overpotential of 670 mV), which is three times larger than that of WO₃ (5.1 mA cm⁻²). No Ir or Ru was detectable after the OER operation of the catalysts (Supporting Information Figure S9). Furthermore, the carbon paper

(CP) showed negligible oxidation current, indicating that the OER activity came from WO₃ itself. It should be noted that the presence of vacancies modified the electronic structure that not only altered the interactions of surface W and OER intermediates, as revealed by the DFT calculations but also improved the conductivity. As a result, the WO₃-Vₒ exhibited a smaller charge-transfer resistance than that of WO₃ (Supporting Information Figure S10). Besides, the oxygen vacancies also provided more coordinately unsaturated sites that led to a larger electrochemically active surface area (ECSA) of the WO₃-Vₒ (Supporting Information Figure S11). However, this difference (543 vs 314 cm²) could not account fully for the dramatically enhanced performance of WO₃-Vₒ. Indeed, the WO₃-Vₒ still showed much larger OER currents than WO₃ after being normalized by ECSA. For example, the current density of WO₃-Vₒ at 1.90 V versus RHE was 2.4 times as large as that of WO₃ (0.038 vs 0.016 mA cm⁻² per ECSA, Supporting Information Figure S11). Similarly, the WO₃-Vₒ also showed much larger Brunauer–Emmett–Teller (BET) surface area normalized OER currents than WO₃ (Supporting Information Figure S12), suggesting the enhancement of intrinsic
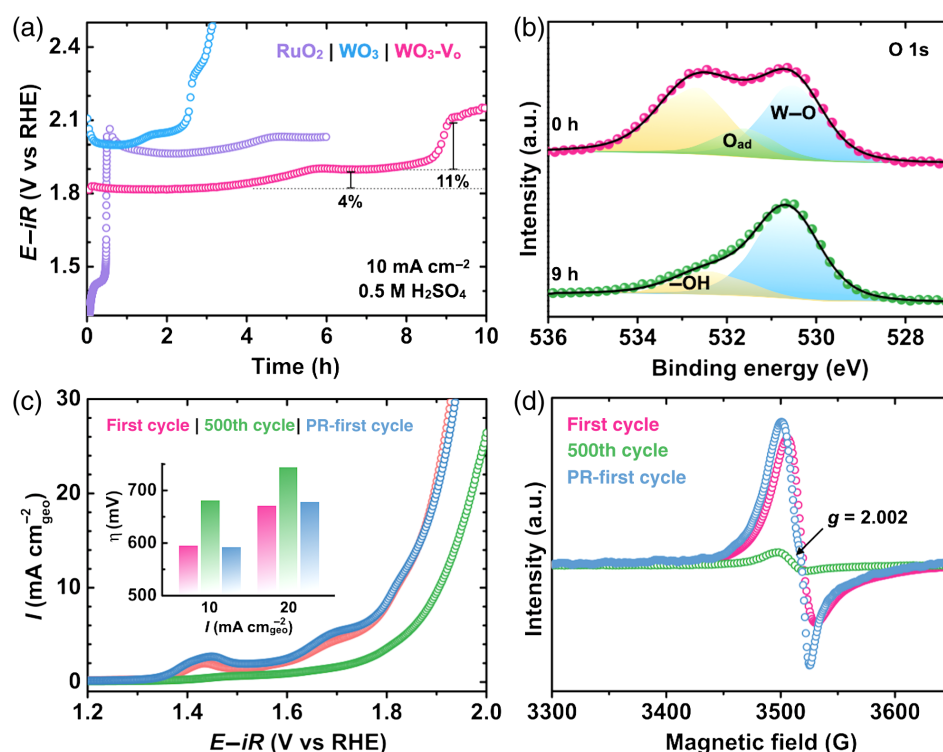
Figure 3. | *Plasma regeneration of oxygen vacancies enables the reuse of WO_3-V_O for OER in 0.5 M H_2SO_4. (a) Chronopotentiometric curves collected at 10 mA cm^{-2}. (b) O 1s XPS spectra evolution of WO_3-V_O upon the OER electrocatalysis. (c) LSV curves of WO_3-V_O and WO_3-V_O-PR recorded after different CV cycles. Inset shows the comparison of overpotentials at different current densities. (d) EPR spectra of WO_3-V_O and WO_3-V_O-PR at different CV cycles.*

activity by vacancy engineering. This was supported further by the O_2 turnover frequency (TOF) calculation result. As shown in Figure 2f, the average TOF of the WO_3-V_O is four to eight times as large as that of WO_3 in the potential region of 1.8–2.0 V versus RHE. Furthermore, the WO_3-V_O also possessed a much smaller Tafel slope (183.3 mV dec^{-1}) than that of WO_3 (280.1 mV dec^{-1}; Supporting Information Figure S13). These observations confirmed the predictions from DFT results and suggested that the WO_3-V_O is an effective electrocatalyst for OER in acidic media, though the WO_3 had poor activity. The overpotentials of WO_3-V_O and WO_3 at 10 mA cm^{-2} were 590 and 770 mV, respectively, close to the calculated result (500 and 750 mV). Although the overpotentials were 130–250 mV larger than the that of state-of-the-art OER catalysts (i.e., IrO_x and RuO_x), the WO_3-V_O had already outperformed many recently reported acidic OER catalysts, including some noble metal-based compounds such as Pt/C at a significantly reduced cost of WO_3-Vo being only ~1/250 and 1/1200 of IrO_x or RuO_x, respectively (Figure 2g and Supporting Information Table S1).

Furthermore, we examined the stability of WO_3-V_O by operating the OER at a constant current density of 10 mA cm^{-2}. As demonstrated in Figure 3a (and

Supporting Information Figure S14), although the initial potential of RuO_2 is quite low, it rises quickly from ~1.45 to 2.0 V versus RHE in 30 min, essentially losing its activity. This result is in agreement with previous reports that the RuO_2 suffered from poor long-term stability, despite its high initial activity.[45–47] The WO_3 was almost inactive for OER and required a high initial overpotential of 770 mV (vs 2.0 V RHE) at 10 mA cm^{-2}, and the potential sharply raised to higher than 2.5 V versus RHE after 3 h. In contrast, the WO_3-V_O was stable for at least 6 h, which was already 12 times as long as that of RuO_2. In fact, this number (operation time) is among the best-reported values of OER electrocatalysts achieved in acidic media (see the comparison in Supporting Information Table S1). Interestingly, we noted that during the OER catalysis, the surface color of WO_3-V_O changed gradually from deep blue to light green, maintaining the same color as WO_3. This observation indicated that the surface vacancies of WO_3-V_O had been filled though its bulk structure remained the same (Supporting Information Figure S15), which is likely responsible for the activity loss in WO_3.

Then we employed XPS to track the surface oxygen species and found that the original O 1s peak at 531.7 eV that is associated with oxygen vacancies disappeared

after the electrocatalysis (Figure 3b). The surface W^{5+} in WO_3-V_O had also been oxidized to W^{6+} (Supporting Information Figure S15), further confirming the filling of oxygen vacancies upon the OER. This result revealed that the electronicproperty of WO_3-V_O after the OER was essentially similar to that of pristine WO_3. Furthermore, the nanowire morphology was observed to be retained mainly though a slight surface aggregation. This is different from that of WO_3, which underwent a more severe aggregation (Supporting Information Figure S16). As we demonstrated earlier, the vacancy engineering could effectively tune the electronic properties, and subsequently, boost the OER activity substantially. This finding provided us with an excellent opportunity to reactivate the WO_3-V_O-OER by regenerating the oxygen vacancies, especially given the highly reserved nanowire structures. Therefore, we conducted a second plasma treatment (30 s) on the catalyst and investigated further the OER performance of the plasma reactivated WO_3-V_O-OER (WO_3-V_O-PR; see the structural characterization in Supporting Information Figure S17). As shown in Figure 3c, the activity of WO_3-V_O gradually decays upon cycling. The overpotential at 10 mA cm^{-2} increases from 590 to 675 mV after 500 continuous cyclic voltammetry (CV) cycles. While after plasma reactivation, the activity is recovered, and the overpotential drops back to 587 mV. A similar trend is again observed for the overpotential required at 20 mA cm^{-2}, further confirming the efficacy of our strategy. Here, we showed for the first time that catalysts could be reused upon specific simple treatments. To confirm the activity of WO_3-V_O-PR indeed originated from the oxygen vacancies, we carried out EPR analysis, and the results show that all samples possess an EPR signal at $\sim g = 2.002$ (Figure 3d), indicative of electrons trapping at vacancy sites.[39] Compared with WO_3-V_O-OER (after 500 CV cycles), both the WO_3-V_O and WO_3-V_O-PR possessed much stronger peak intensities, manifesting higher concentrations of vacancies. The simple and fast plasma reactivation prolonged the lifespan of the catalyst considerably without sacrificing the OER activity while avoiding the tedious and costly synthesis process, which significantly lowered the overall cost and greatly enhanced the catalyst utilization efficiency.

Furthermore, we probed the evolution of oxygen vacancies during the OER catalysis by performing a synchrotron X-ray absorption fine structure (XAFS) analysis. Figure 4a displays the X-ray absorption near edge structure (XANES) spectra at the W L$_3$ edge of WO_3, WO_3-V_O, WO_3-V_O-OER, and WO_3-V_O-PR. The normalized spectra of all the four samples exhibit a broad white-line absorption because of the electronic dipole transitions from W $2p_{3/2}$ to mainly 5d orbitals.[48,49] Though the spectral profiles are similar to each other, subtle differences among the samples are already visible in detailed comparisons of their while-line peaks (top-left inset of

Figure 4a), revealing the difference in W local symmetry and electronic structure. The WO_3 exhibits the strongest intensity, suggesting the high symmetry of the local structure. The WO_3-V_O and WO_3-V_O-PR, in contrast, possess much weak intensities, which suggests the increased distortion of WO_6 octahedra because of the oxygen vacancies. The peak intensity of WO_3-V_O-OER is higher than WO_3-V_O, but it is still lower than that of WO_3, indicating that some of the oxygen vacancies survived even after the OER. This result is consistent with the EPR analysis, where the WO_3-V_O-OER still shows a weak signal, likely because the oxygen vacancies in the subsurface did not participate in the OER catalysis, given the reaction only occurred at/near the catalyst surface. The presence of vacancies led to a decrease in the W oxidation state, which was confirmed further by the E_O value. The top-right inset of Figure 4a compares the E_O value of the four samples, and the result reveals that the E_O value of WO_3-V_O and WO_3-V_O-PR is smaller than that of WO_3 and WO_3-V_O-OER, indicating that the valence of W decreased as the vacancy concentration increased. The bottom panel of Figure 4a displays the second derivative curves of the XANES spectra, which provides further information on the W 5d orbitals splitting. All the spectra exhibit lower and higher energy minima, corresponding to the splitting of the W 5d into t_{2g} and e_g states. The splitting is $\sim$4.8 eV for WO_3, which decreases to 4.4 eV for WO_3-V_O-PR. This smaller splitting value is attributable to the disordered local structure, as well as the contribution of the uncoordinated W and O atoms.[48] These
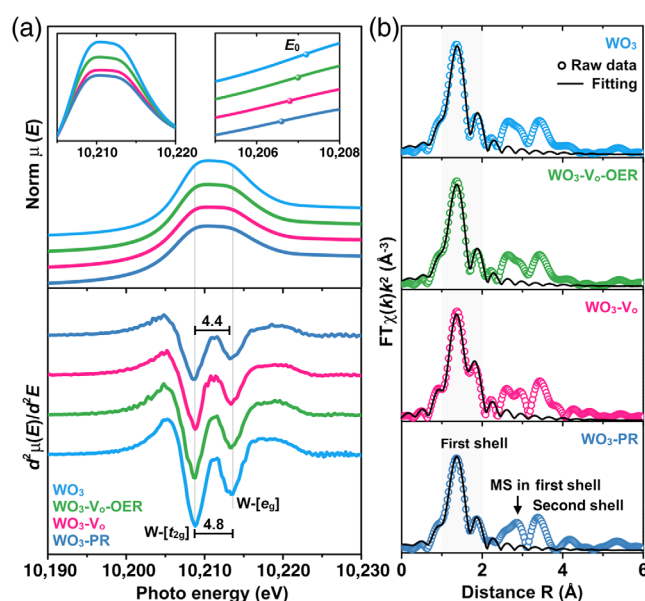
Figure 4. | *XAFS analysis of various WO_3-based catalysts. (a) Normalized W L$_3$-edge XANES spectra (up panel) and their second derivative d^{2}μ(E)/d^{2}E (bottom panel). (b) FT of EXAFS spectra of W L$_3$ an edge.*

results confirm the generation of oxygen vacancies by plasma and their loss after the OER. Figure 4b displays the Fourier transform (FT) of extended XAFS (EXAFS) spectra. The three intense peaks correspond to the single scattering (SS; at 0.7–1.8 Å), the multiple scattering (MS; at 2.2–3.1 Å) in the first shell, and the combined SS and MS signals in the second shell (at 3.1–3.9 Å), respectively.[49,50] Notably, these peak positions are not necessarily the exact crystallographic values.[51] Therefore, we further performed a curve fitting analysis to obtain the structural parameters. In the hexagonal WO_3 structure, the corner-sharing WO_6 octahedra build up three-dimensional (3D) frameworks with hexagonal channels.[52] There are two W–O bonds with different lengths (1.80 and 2.05 Å) in an octahedron. The fitting result reveals that the W atoms in WO_3-Vo-OER have a coordination number close to that of WO_3 (i.e., 5.9 vs 6.0; see Supporting Information Table S2), suggesting the high symmetry of the WO_6 in both samples. In contrast, the coordination numbers of W atoms in WO_3-V_o and WO_3-V_o-PR are much lower (5.4 and 5.3, respectively), which indicates a disordered local structure. Specifically, the W atoms in W–O bond with shorter length have a lower coordination number, identifying the main location of oxygen vacancies. This result agrees well with the XPS and EPR analyses, confirming the introduction of the oxygen vacancies by plasma and the loss of vacancies upon OER electrocatalysis. Together with the structural and electrochemical characterizations, the XAFS analysis strongly supports the critical role of oxygen vacancies in enhancing the OER activity of WO_3-V_o.

In conclusion, we suggest a simple strategy that enables the turning of electrocatalytically inactive materials into efficient *acidic OER* catalysts through plasma-assisted vacancy engineering. We have shown that introducing oxygen vacancies regulates the surface interactions of electrocatalysts and the OER intermediates, hence greatly improving the OER energetics and consequenly boosting the OER activity. As a result, we demonstrate both theoretically and experimentally that WO_3, an acid-stable material with intrinsically poor OER catalytic activity, is able to stably drive an OER current of 10 mA cm^{-2} at an overpotential of 590 mV for at least 6 h. Though the catalytic activity is still inferior to IrO_2 and RuO_2, W is much more abundant, and the cost is only ~1/1200 times as that of Ir. Furthermore, we have shown for the first time that the WO_3-V_o catalyst, after OER, could be reactivated by simple plasma retreatment. This prolongs the lifespan of the catalysts while avoiding the repetitive synthesis process, and hence, significantly reduces the overall cost, which is practically important for the water electrolysis industry. Our work points to a new direction of using defect chemistry to discover inexpensive, efficient, and acid-stable OER catalysts, which potentially could be used for large-scale water electrolysis and other OER involved applications.

Supporting Information

Supporting Information is available.

Conflict of Interest

There is no conflict of interest to report.

Acknowledgments

References

1. Sardar K.; Petrucco E.; Hiley C. I.; Sharman J. D.; Wells P. P.; Russell A. E.; Kashtiban R. J.; Sloan J.; Walton R. I. Water-Splitting Electrocatalysis in Acid Conditions Using Ruthenate-Iridate Pyrochlores. *Angew. Chem. Int. Ed*. **2014**, *53*, 10960–10964.
2. O'hayre R.; Cha S.-W.; Colella W.; Prinz F. B. *Fuel Cell Fundamentals*; John Wiley & Sons: New Jersey, USA, **2016**.
3. Carmo M.; Fritz D. L.; Mergel J.; Stolten D. A Comprehensive Review on PEM Water Electrolysis. *Int. J. Hydrogen Energy* **2013**, *38*, 4901–4934.
4. Shan J.; Zheng Y.; Shi B.; Davey K.; Qiao S.-Z. Regulating Electrocatalysts via Surface and Interface Engineering for Acidic Water Electrooxidation. *ACS Energy Lett*. **2019**, *4*, 2719–2730.
5. Liang H.; Meng F.; Cabán-Acevedo M.; Li L.; Forticaux A.; Xiu L.; Wang Z.; Jin S. Hydrothermal Continuous Flow Synthesis and Exfoliation of NiCo Layered Double Hydroxide Nanosheets for Enhanced Oxygen Evolution Catalysis. *Nano Lett*. **2015**, *15*, 1421–1427.
6. Liang H.; Gandi A. N.; Anjum D. H.; Wang X.; Schwingenschlögl U.; Alshareef H. N. Plasma-Assisted Synthesis of NiCoP for Efficient Overall Water Splitting. *Nano Lett*. **2016**, *16*, 7718–7725.
7. McCrory C. C.; Jung S.; Ferrer I. M.; Chatman S. M.; Peters J. C.; Jaramillo T. F. Benchmarking Hydrogen Evolving Reaction and Oxygen Evolving Reaction Electrocatalysts for Solar Water Splitting Devices. *J. Am. Chem. Soc*. **2015**, *137*, 4347–4357.
8. Shi H.; Liang H.; Ming F.; Wang Z. Efficient Overall Water Splitting Electrocatalysis Using Lepidocrocite VOOH Hollow Nanospheres. *Angew. Chem. Int. Ed*. **2017**, *56*, 573–577.
9. Liang H.; Gandi A. N.; Xia C.; Hedhili M. N.; Anjum D. H.; Schwingenschlögl U.; Alshareef H. N. Amorphous NiFe-OH/NiFeP Electrocatalyst Fabricated at Low Temperature for Water Oxidation Applications. *ACS Energy Lett*. **2017**, *2*, 1035–1042.

10. Fang Z.; Peng L.; Qian Y.; Zhang X.; Xie Y.; Cha J. J.; Yu G. Dual Tuning of Ni–Co–A (A = P, Se, O) Nanosheets by Anion Substitution and Holey Engineering for Efficient Hydrogen Evolution. *J. Am. Chem. Soc.* **2018**, *140*, 5241–5247.

11. Fang Z.; Peng L.; Lv H.; Zhu Y.; Yan C.; Wang S.; Kalyani P.; Wu X.; Yu G. Metallic Transition Metal Selenide Holey Nanosheets for Efficient Oxygen Evolution Electrocatalysis. *ACS Nano* **2017**, *11*, 9550–9557.

12. Seitz L. C.; Dickens C. F.; Nishio K.; Hikita Y.; Montoya J.; Doyle A.; Kirk C.; Vojvodic A.; Hwang H. Y.; Norskov J. K. A Highly Active and Stable $IrO_x/SrIrO_3$ Catalyst for the Oxygen Evolution Reaction. *Science* **2016**, *353*, 1011–1014.

13. Neri G.; Aldous I. M.; Walsh J. J.; Hardwick L. J.; Cowan A. J. A Highly Active Nickel Electrocatalyst Shows Excellent Selectivity for CO_2 Reduction in Acidic Media. *Chem. Sci.* **2016**, *7*, 1521–1526.

14. Chen S.; Perathoner S.; Ampelli C.; Mebrahtu C.; Su D.; Centi G. Room-Temperature Electrocatalytic Synthesis of NH_3 from H_2O and N_2 in a Gas–Liquid–Solid Three-Phase Reactor. *ACS Sustain. Chem. Eng.* **2017**, *5*, 7393–7400.

15. Nave M. I.; Kornev K. G. Complexity of Products of Tungsten Corrosion: Comparison of the 3D Pourbaix Diagrams with the Experimental Data. *Metall. Mater. Trans. A* **2017**, *48*, 1414–1424.

16. Zhu T.; Chong M. N.; Chan E. S. Nanostructured Tungsten Trioxide Thin Films Synthesized for Photoelectrocatalytic Water Oxidation: A Review. *ChemSusChem* **2014**, *7*, 2974–2997.

17. Huang Z. F.; Song J.; Pan L.; Zhang X.; Wang L.; Zou J. J. Tungsten Oxides for Photocatalysis, Electrochemistry, and Phototherapy. *Adv. Mater.* **2015**, *27*, 5309–5327.

18. Zheng T.; Sang W.; He Z.; Wei Q.; Chen B.; Li H.; Cao C.; Huang R.; Yan X.; Pan B. Conductive Tungsten Oxide Nanosheets for Highly Efficient Hydrogen Evolution. *Nano Lett.* **2017**, *17*, 7968–7973.

19. Hu G.; Li J.; Liu P.; Zhu X.; Li X.; Ali R. N.; Xiang B. Enhanced Electrocatalytic Activity of WO₃@NPRGO Composite in a Hydrogen Evolution Reaction. *Appl. Surf. Sci.* **2019**, *463*, 275–282.

20. Chen J.; Yu D.; Liao W.; Zheng M.; Xiao L.; Zhu H.; Zhang M.; Du M.; Yao J. WO_{3-x} Nanoplates Grown on Carbon Nanofibers for an Efficient Electrocatalytic Hydrogen Evolution Reaction. *ACS Appl. Mater. Interfaces* **2016**, *8*, 18132–18139.

21. Zhang B.; Zheng X.; Voznyy O.; Comin R.; Bajdich M.; García-Melchor M.; Han L.; Xu J.; Liu M.; Zheng L. Homogeneously Dispersed Multimetal Oxygen-Evolving Catalysts. *Science* **2016**, *352*, 333–337.

22. Bajdich M.; García-Mota M.; Vojvodic A.; Nørskov J. K.; Bell A. T. Theoretical Investigation of the Activity of Cobalt Oxides for the Electrochemical Oxidation of Water. *J. Am. Chem. Soc.* **2013**, *135*, 13521–13530.

23. Liao P.; Keith J. A.; Carter E. A. Water Oxidation on Pure and Doped Hematite (0001) Surfaces: Prediction of Co and Ni as Effective Dopants for Electrocatalysis. *J. Am. Chem. Soc.* **2012**, *134*, 13296–13309.

24. Yan D.; Li Y.; Huo J.; Chen R.; Dai L.; Wang S. Defect Chemistry of Nonprecious Metal Electrocatalysts for Oxygen Reactions. *Adv. Mater.* **2017**, *29*, 1606459.

25. Asnavandi M.; Yin Y.; Li Y.; Sun C.; Zhao C. Promoting Oxygen Evolution Reactions Through Introduction of Oxygen Vacancies to Benchmark NiFe–OOH Catalysts. *ACS Energy Lett.* **2018**, *3*, 1515–1520.

26. Chen X.; Yu M.; Yan Z.; Guo W.; Fan G.; Ni Y.; Liu J.; Zhang W.; Xie W.; Cheng F. Boosting Electrocatalytic Oxygen Evolution by Cation Defect Modulation via Electrochemical Etching. *CCS Chem.* **2020**, *2*, 675–685.

27. Gillet M.; Lemire C.; Gillet E.; Aguir K. The Role of Surface Oxygen Vacancies upon WO₃ Conductivity. *Surf. Sci.* **2003**, *532*, 519–525.

28. Zhai T.; Xie S.; Yu M.; Fang P.; Liang C.; Lu X.; Tong Y. Oxygen Vacancies Enhancing Capacitive Properties of MnO_2 Nanorods for Wearable Asymmetric Supercapacitors. *Nano Energy* **2014**, *8*, 255–263.

29. Zhu Y.-P.; Xia C.; Lei Y.; Singh N.; Schwingenschlögl U.; Alshareef H. N. Solubility Contrast Strategy for Enhancing Intercalation Pseudocapacitance in Layered MnO_2 Electrodes. *Nano Energy* **2019**, *56*, 357–364.

30. Lu X.; Zeng Y.; Yu M.; Zhai T.; Liang C.; Xie S.; Balogun M. S.; Tong Y. Oxygen Deficient Hematite Nanorods as High Performance and Novel Negative Electrodes for Flexible Asymmetric Supercapacitors. *Adv. Mater.* **2014**, *26*, 3148–3155.

31. Peterson A. A.; Abild-Pedersen F.; Studt F.; Rossmeisl J.; Nørskov J. K. How Copper Catalyzes the Electroreduction of Carbon Dioxide into Hydrocarbon Fuels. *Energy Environ. Sci.* **2010**, *3*, 1311–1315.

32. Rodriguez J. A.; Hanson J. C.; Frenkel A. I.; Kim J. Y.; Pérez M. Experimental and Theoretical Studies on the Reaction of H_2 with NiO: Role of O Vacancies and Mechanism for Oxide Reduction. *J. Am. Chem. Soc.* **2002**, *124*, 346–354.

33. Dou S.; Tao L.; Wang R.; El Hankari S.; Chen R.; Wang S. Plasma-Assisted Synthesis and Surface Modification of Electrode Materials for Renewable Energy. *Adv. Mater.* **2018**, *30*, 1705850.

34. Ouyang B.; Zhang Y.; Xia X.; Rawat R. S.; Fan H. J. A Brief Review on Plasma for Synthesis and Processing of Electrode Materials. *Mater. Today Nano* **2018**, *3*, 28–47.

35. Wang Z.; Zhang Y.; Neyts E. C.; Cao X.; Zhang X.; Jang B. W.-L.; Liu C.-j. Catalyst Preparation with Plasmas: How Does It Work? *ACS Catal.* **2018**, *8*, 2093–2110.

36. Liang H.; Ming F.; Alshareef H. N. Applications of Plasma in Energy Conversion and Storage Materials. *Adv. Energy Mater.* **2018**, *8*, 1801804.

37. Sun Y.; Liu Q.; Gao S.; Cheng H.; Lei F.; Sun Z.; Jiang Y.; Su H.; Wei S.; Xie Y. Pits Confined in Ultrathin Cerium (IV) Oxide for Studying Catalytic Centers in Carbon Monoxide Oxidation. *Nat. Commun.* **2013**, *4*, 2899.

38. Banger K.; Yamashita Y.; Mori K.; Peterson R.; Leedham T.; Rickard J.; Sirringhaus H. Low-Temperature, High-Performance Solution-Processed Metal Oxide Thin-Film Transistors Formed by a 'Sol–Gel on Chip' Process. *Nat. Mater.* **2011**, *10*, 45.

39. Moreno-Hernandez I. A.; MacFarland C. A.; Read C. G.; Papadantonakis K. M.; Brunschwig B. S.; Lewis N. S. Crystalline Nickel Manganese Antimonate as a Stable Water-Oxidation Catalyst in Aqueous 1.0 M H_2SO_4. *Energy Environ. Sci.* **2017**, *10*, 2103–2108.

40 Han L.; Tang P.; Reyes-Carmona A. l.; Rodríguez-García B.; Torréns M.; Morante J. R.; Arbiol J.; Galan-Mascaros J. R. Enhanced Activity and Acid pH Stability of Prussian Blue-Type Oxygen Evolution Electrocatalysts Processed by Chemical Etching. *J. Am. Chem. Soc*. **2016**, *138*, 16037–16045.

41 Bhowmik T.; Kundu M. K.; Barman S. Growth of One-Dimensional RuO$_2$ Nanowires on g-Carbon Nitride: An Active and Stable Bifunctional Electrocatalyst for Hydrogen and Oxygen Evolution Reactions at All Ph Values. *ACS Appl. Mater. Interfaces* **2016**, *8*, 28678–28688.

42 Han N.; Yang K. R.; Lu Z.; Li Y.; Xu W.; Gao T.; Cai Z.; Zhang Y.; Batista V. S.; Liu W. Nitrogen-Doped Tungsten Carbide Nanoarray as an Efficient Bifunctional Electrocatalyst for Water Splitting in Acid. *Nat. Commun.* **2018**, *9*, 924.

43 Zhang N.; Li X.; Ye H.; Chen S.; Ju H.; Liu D.; Lin Y.; Ye W.; Wang C.; Xu Q. Oxide Defect Engineering Enables to Couple Solar Energy into Oxygen Activation. *J. Am. Chem. Soc*. **2016**, *138*, 8928–8935.

44. Grenier J.; Wattiaux A.; Doumerc J.; Dordor P.; Fournes L.; Chaminade J.; Pouchard M. Electrochemical Oxygen Intercalation into Oxide Networks. *J. Solid State Chem*. **1992**, *96*, 20–30.

45. Lin Y.; Tian Z.; Zhang L.; Ma J.; Jiang Z.; Deibert B. J.; Ge R.; Chen L. Chromium-Ruthenium Oxide Solid Solution Electrocatalyst for Highly Efficient Oxygen Evolution Reaction in Acidic Media. *Nat. Commun*. **2019**, *10*, 162.

46. Kim J.; Shih P.-C.; Tsao K.-C.; Pan Y.-T.; Yin X.; Sun C.-J.; Yang H. High-Performance Pyrochlore-Type Yttrium Ruthenate Electrocatalyst for Oxygen Evolution Reaction in Acidic Media. *J. Am. Chem. Soc.* **2017**, *139*, 12076–12083.

47. Miao X.; Zhang L.; Wu L.; Hu Z.; Shi L.; Zhou S. Quadruple Perovskite Ruthenate as a Highly Efficient Catalyst for Acidic Water Oxidation. *Nat. Commun.* **2019**, *10*, 3809.

48. Triana C. A.; Araujo C. M.; Ahuja R.; Niklasson G. A.; Edvinsson T. Disentangling the Intricate Atomic Short-Range Order and Electronic Properties in Amorphous Transition Metal Oxides. *Sci. Rep.* **2017**, *7*, 2044.

49. Yamazoe S.; Hitomi Y.; Shishido T.; Tanaka T. XAFS Study of Tungsten L1-and L3-Edges: Structural Analysis of WO$_3$ Species Loaded on TiO$_2$ as a Catalyst for Photo-Oxidation of Nh3. *J. Phys. Chem. C* **2008**, *112*, 6869–6879.

50. Kuzmin A.; Purans J. X-Ray Absorption Spectroscopy Study of Local Structural Changes in a-WO$_3$ Under Colouration. *J. Phys.: Condens. Matter* **1993**, *5*, 2333.

51. Agondanou J.-H.; Spyroulias G. A.; Purans J.; Tsikalas G.; Souleau C.; Coutsolelos A. G.; Benazeth S. XAFS Study of Gadolinium and Samarium Bisporphyrinate Complexes. *Inorg. Chem.* **2001**, *40*, 6088–6096.

52. Solonin Y. M.; Khyzhun O. Y.; Graivoronskaya E. Non-stoichiometric Tungsten Oxide Based on Hexagonal WO$_3$. *Cryst. Growth Des*. **2001**, *1*, 473–477.